A&A manuscript no.
(will be inserted by hand later)

Your thesaurus codes are:
03.13.2; 03.13.6; 06.07.1

ASTRONOMY
AND
ASTROPHYSICS
3.11.1996

Fourier versus Wavelet Analysis of Solar Diameter Variability

A. Vigouroux and Ph. Delache

Laboratoire Cassini, associé au C.N.R.S. (U.R.A. 1362), Observatoire de la Côte d'Azur, B.P. 229, F-06304 Nice Cedex 4, France

Received date; accepted date

Abstract. Up to now, time dependence of solar radius measurements from the CERGA astrolabe has been analysed through spectral techniques. In the present paper, we compare results obtained in using "wavelet" instead of Fourier transform. We show that this particular data set should better be considered as a sum of wavelets rather than a superposition of stationary oscillations.

Key words: Methods: data analysis – Methods: statistical – Sun: general

Cet article est une version longue de celui qui parut dans Astronomy and Astrophysics **278***, 607-616, en 1993.*

1. Introduction

Measurements of the solar radius have started at Observatoire de la Côte d'Azur in 1975 (Laclare, 1983). Originally, they were aimed at precise astrometric determination of the Sun's motion along the ecliptic. Observations have been obtained by a single observer, F. Laclare, through a visual Danjon astrolabe. Astrometrists are used to collect homogeneous daily data for many years, for they know how much routine observations can be rewarding. The solar diameter was obtained, in the beginning, as a by-product of observations reduction. Along the years, however, it became more and more evident that significant variations were detected in diameter observations. The problem soon arose of the degree of significance of these variations, together with the question of their physical origin(s). The first question has been addressed through several spectral techniques, from simple ones (Delache *et al.*, 1985) to sophisticated analysis such as Gavryusev *et al.* (1991) have applied. The second question is for the moment still unsolved. It should probably be considered in the wider scope of solar variability. For example, a recent paper (Delache *et al.*, 1993a) has shown that diameter measurement variations do correlate with structural global solar parameters, such as the p-mode fundamental frequency or the Cl^{37} neutrino flux.

The present paper describes an attempt to overcome an implicit limitation of spectral analysis interpretation: the assumption that the signal is validly represented by a superposition of standing waves. In other words, Fourier transform does not tell whether or not a piece of data finds its physical origin in superimposed constant amplitude sine waves. It only tells that IF it were built from such waves, THEN those waves would be entirely described by the complex amplitudes of spectral estimates.

Having noticed that the apparent behaviour of the diameter observations exhibit periods of fast variability, together with quieter ones, we propose to make use of "time and frequency" (also called "time and scale") analysis techniques: the wavelet transform. We want to stress at the beginning that this alternate view may also carry its implicit assumptions, namely that the signal is really made from a superposition of elementary wavelets of different scales: indeed, similar to the Fourier case, we can *a priori* be sure that, given an analysing wavelet and whatever the characteristics of the data, we shall always be able to compute a unique wavelet transform representing it. With an adequate choice of the wavelet, the transformation can also be inverted. In complete analogy with the Fourier transform method developed by Gavryusev *et al.* (1991), we shall define criteria for assessing significance levels of transformed quantities prior to inversion.

There will however be a question that we shall ultimately ask to our data: given a number of independent parameters, which representation of the time series has the highest quality ? Or alternately, prescribing a quality level (the definition will be precised in the paper), which representation needs the least number of independent parameters ? Answering this question is the main subject of this paper.

Send offprint requests to: A. Vigouroux

2. Building the time series

The numerical aspects of the methods that we are going to use are best treated when the number of points is an integer power of 2. With the solar radius measurements that we presently have at our disposal, it appears that there are only slightly more than 5000 days between the first and the last day of observation. Furthermore, previous studies have convinced us to use running mean averages over periods of the order of a few months. Thus, quite similarly to analysis presented recently by Gavryusev *et al.* (1994) we have built a 90-day running mean time series that merges all individual measurements, r_l, whatever the zenith angle where they have been obtained. In order to meet the "2^p" requirement, we keep one point every 9 days, so as to obtain of order 5000/9 values, a figure which is reasonably close to $q = 2^9 = 512$. Our basic data time series becomes then $\mathcal{R}_{i,i=1,512}$, corresponding to instants t_i, 9 days apart.

$\mathcal{R}_i$ being the average of all measurements taken between day $t_i - 45$ and day $t_i + 45$, we have now to assess a figure for the corresponding uncertainty σ_i. Each measurement r_l has its own uncertainty σ_l, from which we can compute the uncertainty σ_i for the 3-month average $\mathcal{R}_i$:

$$\sigma_i = \left[\sum_{t_l \in [t_i - 45, t_i + 45]} (\frac{1}{\sigma_l^2}) \right]^{-1/2}$$

A comparison between uncertainties of averages and measurement dispersions is discussed in Delache *et al.* (1993b). These uncertainties appear on Fig. 1 as 1-σ error bars. Some bars are larger, for example in the beginning of the time series where the number of individual observations was not as high as it became later. The error bars are also larger in periods where observations are scarce, which correspond essentially to winter measurements. Notice also that winter measurements are mostly obtained at larger zenith angle (low over the horizon) where images are more likely to be affected by seeing deterioration. In extreme cases, it may happen that no measurement is available for more than three consecutive months. Errors bars are then simply omitted. This is especially visible during the first years of measurements.

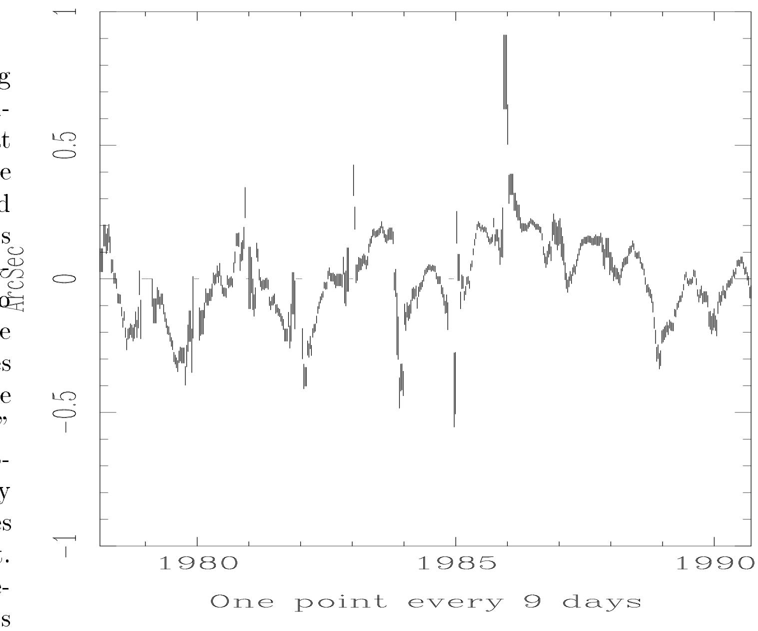

Fig. 1. Solar data observations: 1-σ error bars. Notice larger error bars corresponding to winters, especially in early years.

3. Fourier analysis

We have performed simple numerical finite Fourier transforms (FFT) over the 512 $\mathcal{R}_i$ values. We then obtained 512 numbers arranged as a complex series along increasing frequencies ν_k, from which we may deduce amplitudes of spectral estimates, and eventually recover the original time series exactly (within computer precision) by numerical inversion of the transform. We may also recover some "model" of it, retaining only parts of the spectrum, according to some selection criterium.

Our aim here is not to find very precise values for frequencies, phases, amplitudes of modes deduced from a spectral analysis, such as Gavryusev *et al.* (1991, 1994) have done in a number of cases. However we are going to make use of part of their convincing technique for assessing confidence levels for selection of spectral estimates (Gavryusev *et al.*, 1991).

We describe now the four steps that we have followed.

3.1. Simulation of pure noise

First, we built 200 fake time series containing 512-points. Each individual point is randomly chosen at time t_i from a gaussian distribution of dispersion σ_i, *centered around zero.* In cases where there is no measurement in the original sequence, we set the value precisely equal to zero. We get then 200 possible realizations of observations having the original σ_i characteristics, but shifted as to simulate observing a constant quantity, the constant being zero. In other words we have 200 examples of null observations of the same precision as the real one. From them, we obtain 200 FFT values for the amplitudes a_k at each frequency ν_k. These $200 \times 512 = 102\,400$ points constitute a cloud which mimics the noise induced in the transform by the actual values of σ_i, and also by their temporal repartition. A representation of this cloud, limited to the lower part of the spectrum is shown on Fig. 2, together with the spectrum of the actual original R_i series, drawn to the same scale.

The cloud is adequately represented by a Rayleigh distribution, which is a consequence of the distribution of complex amplitudes being gaussian. Analysis of subsets from the lower to the higher part of the spectrum has not permitted to detect any significant variation of the stan-

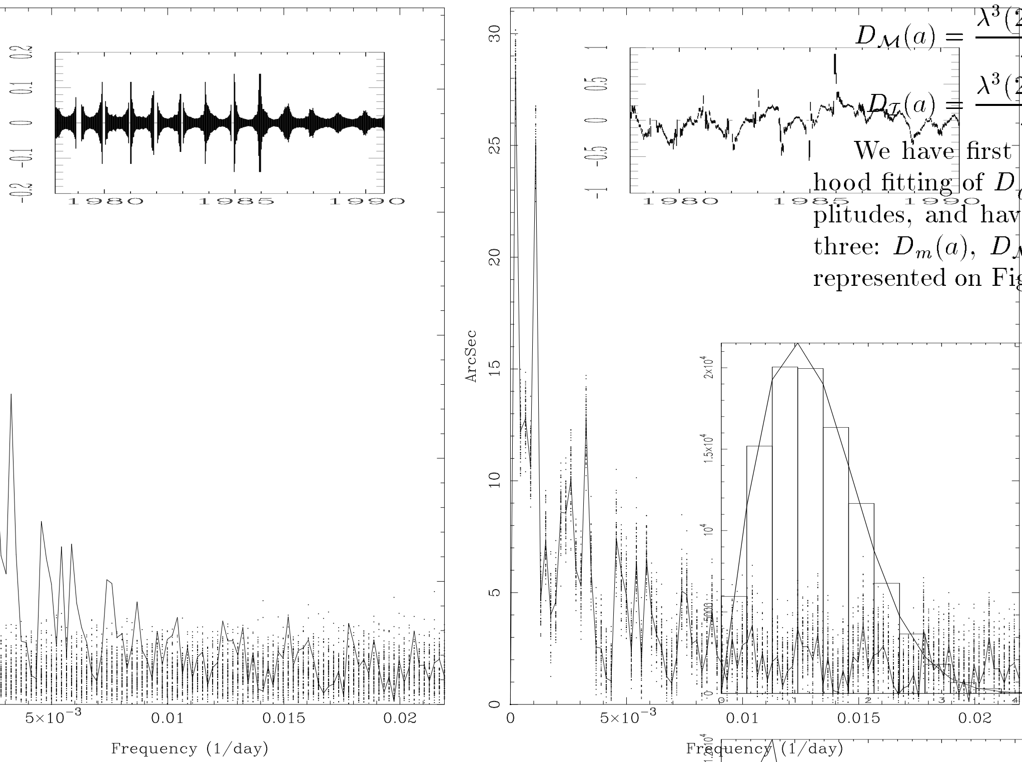

Fig. 2. *Left:* FFT transforms of noise simulation compared to transform of the actual data.
insert: *actual* time series of errors bars centered around zero ;
dots: low frequency part of 200 random spectra of *null* observations; no trend is visible (only 40% of them are represented here).
Right: FFT transforms of randomly simulated data (see text), compared to the transform of the actual data.
insert: *actual* time series of errors bars centered actual data ;
dots: low frequency part of 200 spectra of simulated noisy observations; we have plotted only those points which that are local maximum (only 40% of them are represented here).
solid line: in both case, spectrum of the *original data.*

dard deviation of the distribution. We then define a single σ by fitting all 51 200 amplitudes to the distribution:

$$D_{all}(a) = \lambda a \exp(-\frac{a^2}{2\sigma^2}).$$

We are then in a position to assess 3σ, 4σ, etc.. levels for distribution of amplitudes in any class of points that we would need. For example, from $D_{all}(a)$, assuming independence of neighbouring points in the spectrum, we can deduce the distribution $D_{\mathcal{M}}(a)$ of amplitudes of points $\mathcal{M}$ whose two neighbours are smaller ("maximum"), the distribution $D_m(a)$ of points m whose two neighbours are higher ("minimum"), and also the distribution $D_{\mathcal{I}}(a)$ of points $\mathcal{I}$ which have altogether a smaller neighbour, and a larger one. These distributions are given by:

$$D_m(a) = \frac{\lambda^3(2\sigma^2)^2}{4} a \exp(-\frac{3a^2}{2\sigma^2}).$$

$$D_{\mathcal{M}}(a) = \frac{\lambda^3(2\sigma^2)^2}{4} a \exp(-\frac{a^2}{2\sigma^2})[1-\exp(-\frac{a^2}{2\sigma^2})]^2.$$

$$D_{\mathcal{I}}(a) = \frac{\lambda^3(2\sigma^2)^2}{4} a \exp(-\frac{2a^2}{2\sigma^2})[1-\exp(-\frac{a^2}{2\sigma^2})].$$

We have first computed σ through maximum likelyhood fitting of $D_{all}(a)$ to the actual distribution of amplitudes, and have further used it's value for the other three: $D_m(a)$, $D_{\mathcal{M}}(a)$, and $D_{\mathcal{I}}(a)$. All distributions are represented on Fig. 3.

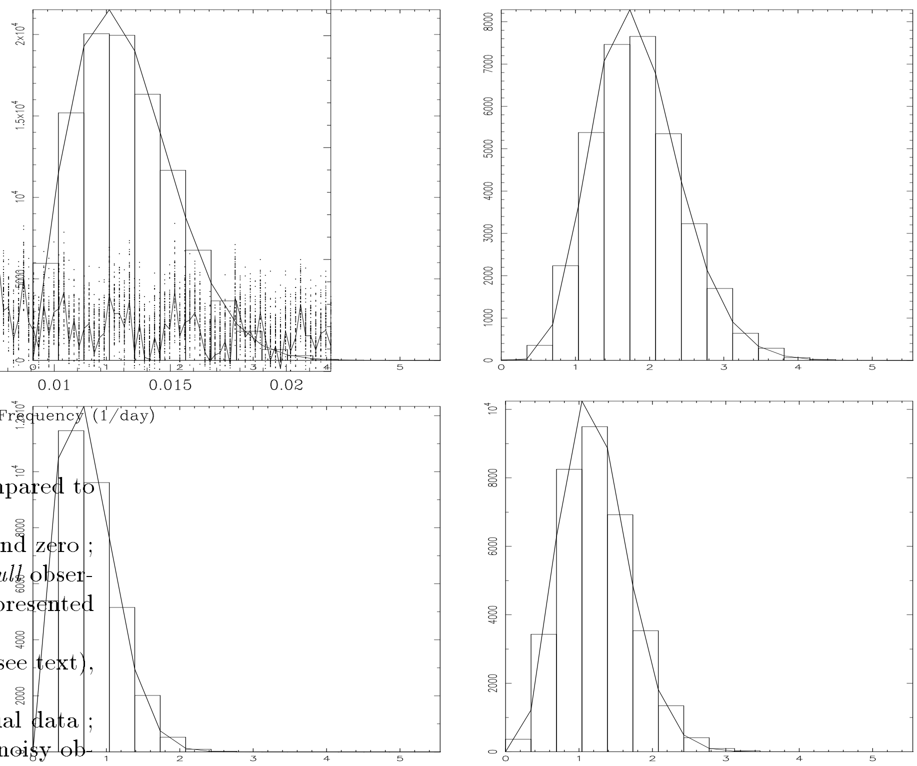

Fig. 3. Distributions of spectral estimates amplitudes; the x-axis are labeled in unit of σ as deduced from the gaussian fit $D_{all}(a)$.
boxes: histogram of from 200 realizations
solid lines: functional fits
top: distributions $D_{all}(a)$ & $D_{\mathcal{M}}(a)$
bottom: distributions $D_m(a)$ & $D_{\mathcal{I}}(a)$
It can be verified that fits are as good for $D_{\mathcal{M}}(a)$, $D_m(a)$ and $D_{\mathcal{I}}(a)$ as for $D_{all}(a)$ from which σ has been deduced.

3.2. Simulation of uncertain data

We then calculate another similar 200 random time series, but this time the gaussian distribution is centered *around the actual values* $\mathcal{R}_i$. Examination of the distribution of representative points in individual spectra, especially in the lower part of them where amplitudes are much larger than 3σ shows that maximum (and minimum) do not always appear at the exact frequency where the spectrum of the original data would have shown them (Fig. 2).

We could imagine various reasons for it: a real standing wave is present in the physical phenomenon from which we have obtained measurements, in the vicinity of the frequencies under consideration. Only uncertainties in the observations makes those points flip from one frequency ν_k to a neighbouring one in different realizations. Alternatively, it may be that, if we have had more precision and extended observational length, the spectrum would still exhibit the same wide feature, such as a dampen harmonic oscillation or very close standing waves could produce; then flip of the same kind could happen, induced also by uncertainties in the observations - but smaller ones could then suffice. As we have already said in the introduction, the data cannot decide, and we shall not decide either. We shall instead concentrate only on the statistical information. At this point, our analysis differs from Gavryusev *et al.* (1991) "cluster" procedure. Let us briefly comment their approach. When one has the *a priori* idea of searching for standing sinusoidal waves, then the Fourier analysis is the ideal tool. Instead of taking in the spectra the points $\mathcal{M}$, $\mathcal{I}$ and m they have done their work on, first, local maximum points $\mathcal{M}$, and second, on those points $\mathcal{N}$ which have altogether a smaller neighbour, and a larger one which is a local maximum $\mathcal{M}$. They have oversampled the spectrum around points $\mathcal{M}$ and $\mathcal{N}$ where there is some significant power. Some organisation of several subsets of the cloud shows up, which are the Gavryusev *et al.* "clusters". They proceed then to a more refined analysis of the structures, eventually leading to improved values of amplitudes, frequencies and phases. Our aim is different here, since we want to produce and test *a model, reconstructed from that part of the transformed data which we find to be significant.*

3.3. Thresholding

We then fix a "$n\sigma$" level for the spectral amplitudes above which we shall retain the information. For each frequency ν_k, we have 200 spectral estimates. We select all of them which are $\mathcal{M}$, and keep them if their average passes the $n\sigma$-maximum test in the $D_{\mathcal{M}}$ distribution. We then select all of the m (respectively $\mathcal{I}$) amplitudes and submit them to the same test in the D_m (respectively $D_{\mathcal{I}}$) distribution. Then we compute, for each frequency, how many of the 200 spectra would contribute significantly, either as $\mathcal{M}$, or as m or as $\mathcal{I}$. Fair enough, it appears that the result is very clear: very often (of order 75% of the cases), we find zero, or 200: this means that, given a σ level, when amplitudes at a given frequency ν_k are significant, it happens most of the time that they keep their significance, even if from one random realization to another they evolve between $\mathcal{M}$, m and $\mathcal{I}$ types. So we feel entitled to strengthen even more our selection criterion by taking as significant only those frequencies ν_k where all 200 spectra contribute. This defines a set $\mathcal{K}(\sigma)$ of the selected indexes k. We then take the (complex) average of the 200 values as a good representation of the complex amplitude c_k at the frequencies $\nu_{k,\, k\in\mathcal{K}}$. We consider the amplitudes c_k at other frequencies $\nu_{k,\, k\notin\mathcal{K}}$ to be insignificant and set them equal to zero.

We consider now the number $F(\sigma)$ of (complex) elements in $\mathcal{K}$ that we have retained for reconstructing the signal as a function of the σ value defining our selection level. Figure 4 presents a graph of $F(\sigma)$. We notice that, after a sharp decrease, F is leveling towards a plateau, which it reaches around 5σ. For reference, the same figure shows also the behaviour of F when calculated from purely random realizations of null observations. We may notice that below the 2σ level, more elements are selected from the null realizations than from the actual data realizations. This simply reflects the highest severity of our selection criterion which was described in the beginning of this section. The leveling above 2σ is thus a clear signature of the progressive encounter of significant frequencies surviving the increase in the discriminating level.

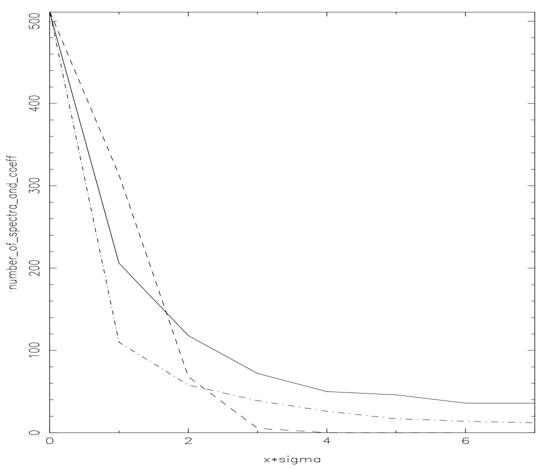

Fig. 4. *solid line*: number $F(\sigma)$ of spectral estimates from actual data, passing a given σ-level significance test; *dashed line*: the same for data built from pure noise; *dashed-dot line*: number $F'(\sigma)$ of coefficients estimates passing a given σ-level significance test, in wavelet analysis.

3.4. Recovering significant part of the original data

We now apply FFT inversions to various sets $\mathcal{K}(\sigma)$ of c_k complex frequencies, selected from different σ-level discriminations. As an example, Fig. 5 shows the result of the inversion (model) that we obtain at the 4.5σ level.

We notice, first, that the model try to reach all points, whatever their intrinsic precisions. This is quite normal, since the σ-level is not frequency dependant, and is thus determined by the *averaged* distribution of uncertainties over the entire series. Second, we may see the effect of imposing a representation built from standing waves: oscillating behaviours appear in places where the original data do not really show them. This is particularly obvious in

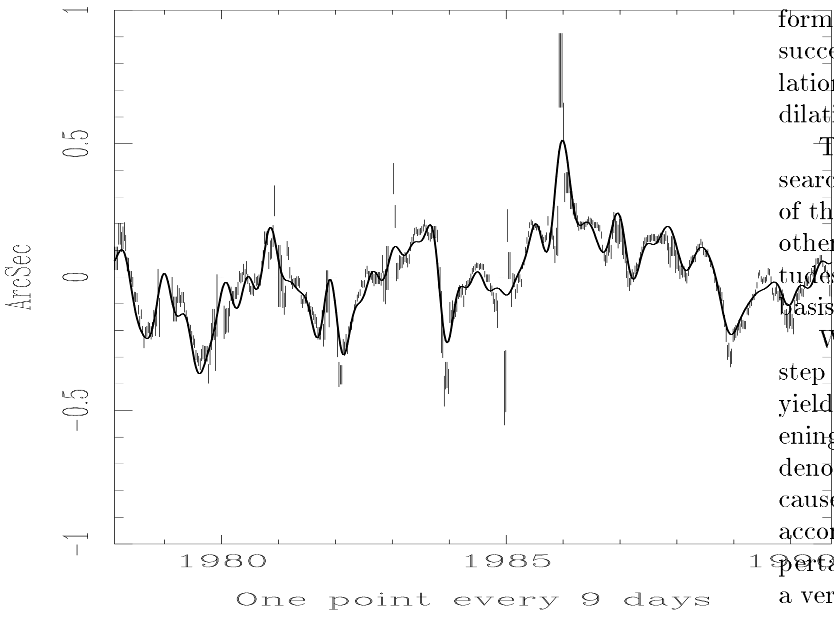

Fig. 5. Result of the FFT inversion with 4.5σ-level in *solid line* with the original data error bars.

locations where, with little or no measurements at all, the reconstructed model sometimes exhibits unexpected short period oscillations. One may also notice the inadequacy of the representation in the 10% ultimate part of the series, where data are numerous and of good, homogeneous quality. Obviously, this comes from behaviours imposed by the previous 90% pieces of data.

4. Wavelet analysis

As we have already seen from the above discussion, we suspect that a representation of the radius data in terms of standing sine waves may not be appropriate. Several sudden increases or decreases in the signal, or some wave packets well localized in time could indeed be spotted on the original $\mathcal{R}_i$ series. We thus need a tool for analysing simultaneously both aspects: time and frequency. But Heisenberg's uncertainty principle tells us that we cannot simultaneously extract precise information on time and frequency of any given "event". The wavelet analysis provides an adequate tool for compromising between time and frequency accuracies.

4.1. Wavelet transform in brief

Let us briefly summarize signal processing by wavelet transform (one can find more information in Grossmann *et al*, 1987, Meyer, 1987, Daubechies, 1987, Bijaoui, 1990, 1991). Whereas Fourier analysis consists in projecting the time series on cosine and sine basis (unlimited in time), wavelet analysis, on the contrary, makes use of a set of "wavelets" which *are localized* in time. The wavelets which form then the basis for projecting the temporal signal are successively generated from the initial one by time translation (which corresponds to time information) and time dilation (which corresponds to frequency information).

The essential idea of the wavelet analysis consists in searching for structures appearing locally similar to one of the translated/expanded original analysing wavelet. In other words, given a wavelet basis, we search for amplitudes of structures obtained from $\mathcal{R}_i$ projected on this basis.

We may associate a frequency band to each dilating step of our wavelet series. Expansion will progressively yields us towards lower frequencies, simultaneously sharpening the frequency band. We shall use the word *scales* to denote the frequency bands associated to each step. Because of the uncertainty principle, time information will accordingly deteriorate: quite naturally, the information pertaining to the lower frequencies will not be attached to a very precise location in time.

In practice, the original data will be decimated from one scale to the next. Starting with our original signal made from 512 equidistant samples, the first step is a projection on a series of translated original wavelets. It provides us with 256 wavelet coefficients of the first kind and leaves a blurred signal of 256 points. The next projection from this blurred 256 points signal on the second scale makes use of a dilated wavelet, and will give us 128 new wavelet coefficients and a further blurred signal of 128 points. And so on, until the last scale where we will obtain a single point signal and the last wavelet coefficient.

As a result, we will have represented our initial $\mathcal{R}_i$ series by it's wavelet coefficients and one ultimate blurred version of it.

4.2. Algorithms for wavelet transforms and processing

We have compared two algorithms for wavelet transform. One of them is known as "algorithm à trou" (hole-algorithm). From the $q = 512$ samples $\mathcal{R}_i$, it provides $q \log_2 q$ wavelet coefficients. It has the advantage of high sensitivity to "events" or well localized discontinuities, which, however, may not be the case for our radius time series. It has the drawback of being sensitive to boundary effects which introduce noise in the reconstruction, which furthermore is not an exact one. So we have preferred using an algorithm which allows exact reconstruction, being a biunivocal relation between the original signal and its wavelet transform; it shares this property with the Fourier transform, thus permitting to follow similar lines in the analysis. It is derived from Mallat, 1989, and has been kindly provided to us by A. Bijaoui. Those filters are associated to the bi-orthogonal wavelet basis, and are represented on Fig. 6. The computation begins, as in the FFT case, with the 512 values R_i. Performing a wavelet transform of this signal yields 9 frequency scales, containing wavelet coefficients plus the last “blurred” signal. From these, it is possible to run the process backwards, thus performing an exact inversion and recovering the original time series.

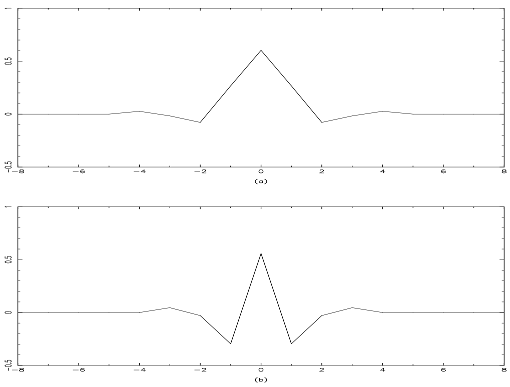

Fig. 6. Shape of the filters used in wavelet analysis.
(a): filter used to calculate the blurred signals;
(b): filter used to calculate the coefficients of the wavelet transform.

We now proceed, as we did in the previous section, from the same 200 fakes 512-point time series, representing 200 realizations of a null observation. We compute the 200 wavelet transforms of those 200 signals. Figure 7 shows coefficients of the first, second and third projections on successive wavelet basis: contrary to the FFT situation, we can readily see the effect of the larger uncertainties σ_i, which induce highest amplitude coefficients. Representing the cloud of points for each wavelet coefficient by a gaussian distribution will permit us to deduce 3σ,..., $n\sigma$ thresholds. It is clear, from the figure, that the assessment of discriminating levels for retaining significant coefficients will be more severe in the vicinity of those points where data are intrinsically more uncertain. We expect then that sorting signal from noise will be more efficient in wavelet space than in Fourier space. The superposed coefficients of the $\mathcal{R}_i$ wavelet transform (solid line) indeed shows that, in several places, those coefficient are buried in the clouds of the random null realizations, in spite of their apparent large amplitudes. This is particularly true in the first scales, which is quite natural, since those scales correspond to the noisier frequency bands.

We then proceed to the computation of the wavelet transforms of the 200 random realizations of the actual $\mathcal{R}_i$ time. On Fig. 8, are plotted the first (256+128+64) coefficients of the first, second and third scales.

Along our previous line, we can now evaluate the 511 discriminating levels, and retain from the 511 coefficients of the wavelet transform of the 200 simulated noisy observations only those which pass the $n\sigma$ tests. The other ones will be set to zero. The effect of such settings is eas-

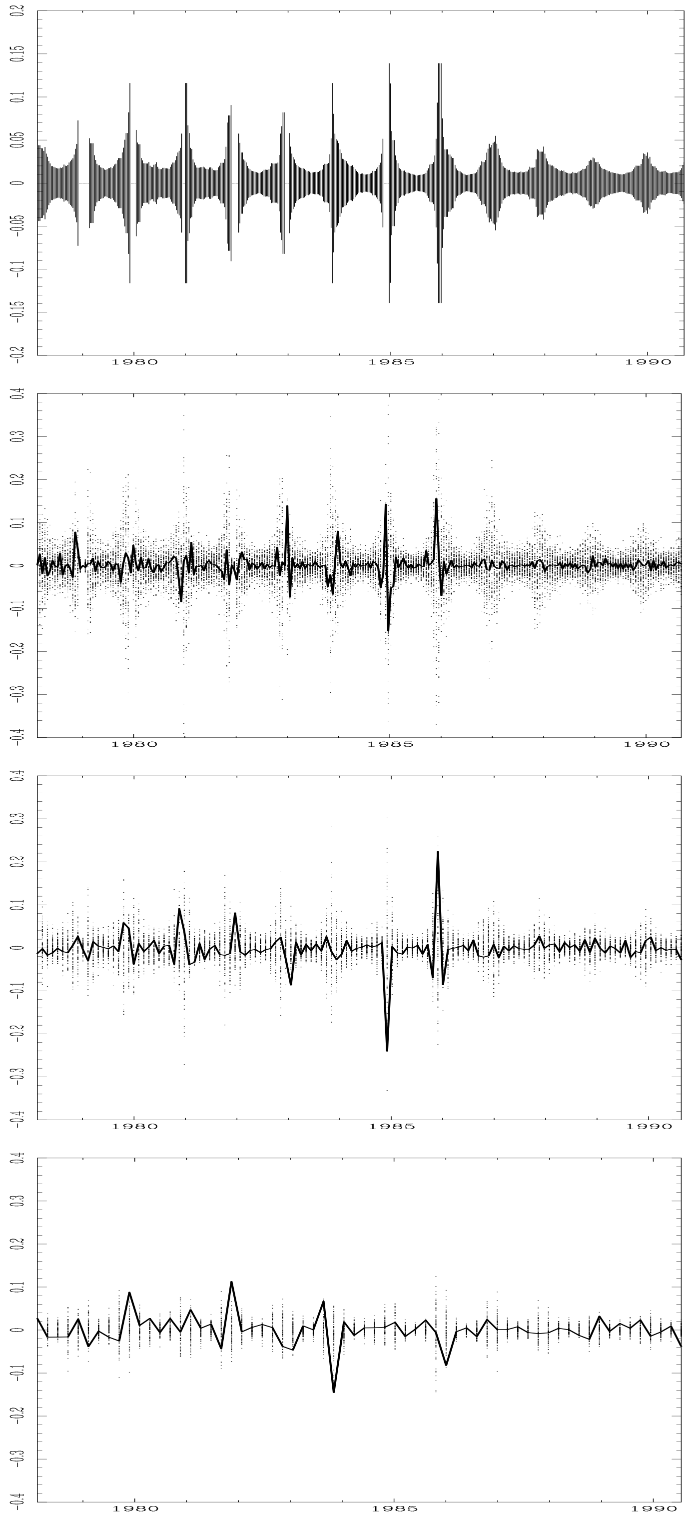

Fig. 7. Wavelet transform of noise simulation compared to transform of the actual data in frequency bands corresponding to the first, second and third scales.
top graph: *actual* times series of errors bars centered around *zero*
following graphs: coefficients of wavelet transforms of 200 random signals corresponding of *null* observations *(dots)* – only 40% being represented here – and coefficients of wavelet transform of $\mathcal{R}_i$ *(solid line)*.

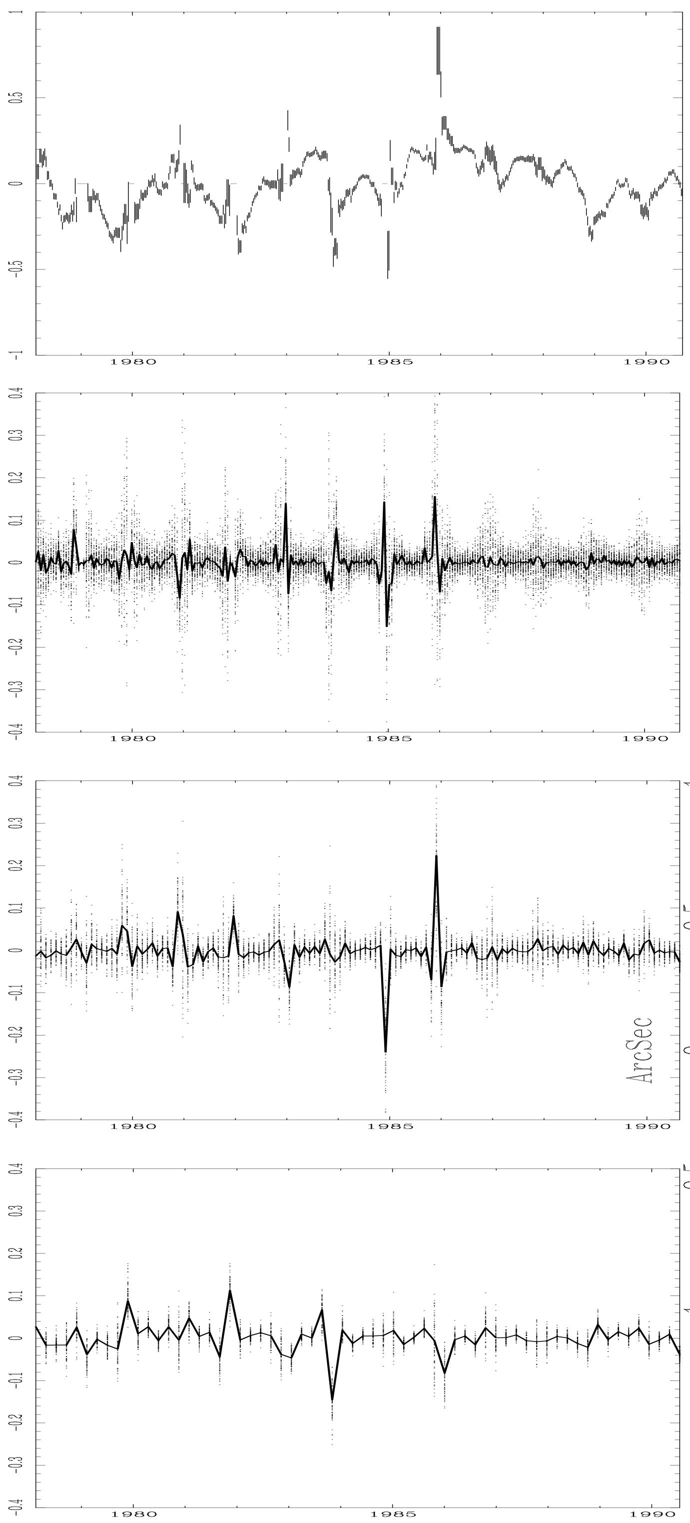

Fig. 8. Wavelet transform of randomly simulated data compared to transform of the actual data in frequency bands corresponding to the first, second, third scales.
top graph: *actual* time series of errors bars centered around *actual* measurements, i.e. same as Fig. 1
following graphs: coefficients of wavelet transform of 200 simulated noisy observations *(dots)* – only 40% being represented here – and coefficients of wavelet transform of $\mathcal{R}_i$ *(solid line)*.

ier to understand in the wavelet space than in the Fourier space: a wavelet coefficient equal to zero means that we choose to consider that no significant "event" is happening around some definite time and some characteristic frequency; whereas in Fourier space, a spectral estimate which is set equal to zero imposes that no standing wave of some definite frequency is significantly fitting the whole series.

4.3. Discussion

Similar to our Fourier analysis, we define the number $\mathcal{F}'(\sigma)$ of surviving coefficients for each threshold. The $\mathcal{F}'(\sigma)$ function is shown on Fig. 4. We notice a faster decrease than in the FFT analysis, but the plateau is also reached around 5σ.

From the average of each selected coefficients taken over the 200 realizations, added to the average of the 200 last blurred signals, we may reconstruct a "filtered" signal, solely built from significant coefficients. The result of an inversion performed through a 3σ-level selection is shown on Fig. 9.

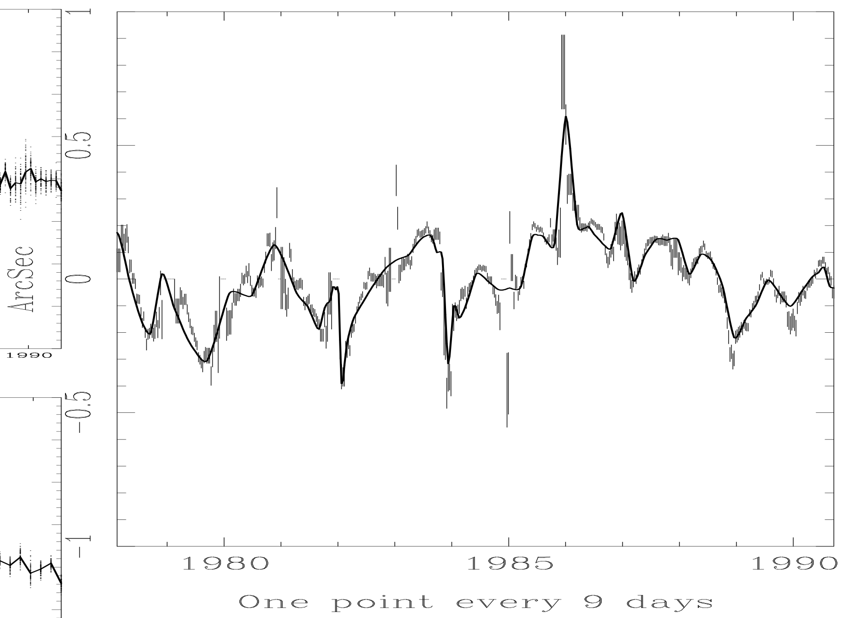

Fig. 9. Result of the wavelet transform inversion with 3σ-level in *solid line* with the errors bars of the original data.

Remembering our considerations on the Fourier reconstruction, we may now consider in some details Fig. 9. We recall first that time uncertainty increases as the frequency band sharpens; second, as we have already noticed, the first scales of the wavelet transform will be the most affected by the $n\sigma$ discrimination. So, it is to be expected that we shall somehow loose the precise temporal information which is recorded in the first scales of the wavelet transform. The Fig. 9 indeed shows this effect: the reconstructed curve follows on the whole correctly the original data, but we can nevertheless notice here and there some imprecision in the location of some rapid variations. As we anticipated, we notice that this reconstruction procedure is efficient in automatic recognition that measurements having large uncertainties should be given little weights.

5. Discussion.

5.1. Overall comparison of merits

We are now able to compare semiquantitatively the two techniques of reconstructing models from the initial time series.

The first, striking property of the wavelet transform technique is its ability to efficiently and automatically recognize the locations where little weight is to be given to imprecise data, which the Fourier scheme is unable to achieve.

Next, and this was of course expected, wavelet transform is able to recognize and reconstruct wave trains, well localized in time. On the contrary, when Fourier analysis is able to do the same, it needs some selection of adjacent frequencies, so as to obtain wave trains by mode beating. This yields to spurious appearance of oscillations in places where obviously they do not represent the original data, or even in places void of data. This can eventually be observed when we apply the wavelet reconstruction technique to the already Fourier-reconstructed time series. Actually, we have done the exercise, in using a 3σ-level discrimination; indeed, we find that the third scale, corresponding to the frequency band $0.0277 day^{-1} - 0.0138 day^{-1}$ now selects as being "significant" several coefficients which were not present in the direct analysis, and which correspond precisely to the spurious wave packets mentioned above.

Finally, as shown on Fig. 4, a comparison of $\mathcal{F}(\sigma)$ with $\mathcal{F}'(\sigma)$ shows that for the time series that we have considered, identical discriminating levels imply significantly less parameters for wavelet reconstruction than for the FFT process.

5.2. Evaluation of the reconstructed models quality

We may also directly compare both reconstructed models with our original data. To this end, we have computed histograms of distances between them at each point t_i where measurements are available. They are shown in Fig. 10. It is immediately visible that gaussian adjustments of these histogram are not suited for fitting altogether the central part and the extended wings. This can easily be interpreted as follow:

At a given σ-level, both techniques try to fit best the original data. Still, one may notice that several points lie far away from the model. These are responsible for the extended wings of the distributions of distances. Increasing the σ-level will leave out higher frequencies in the FFT spectrum (Fig. 2) or wavelet coefficients lying in the finest scale (Fig. 8). In both cases this has the effect of neglecting small groups of points away from a smoothed curve. This also explains why the extended wings are slightly larger in the wavelet-reconstructed model.

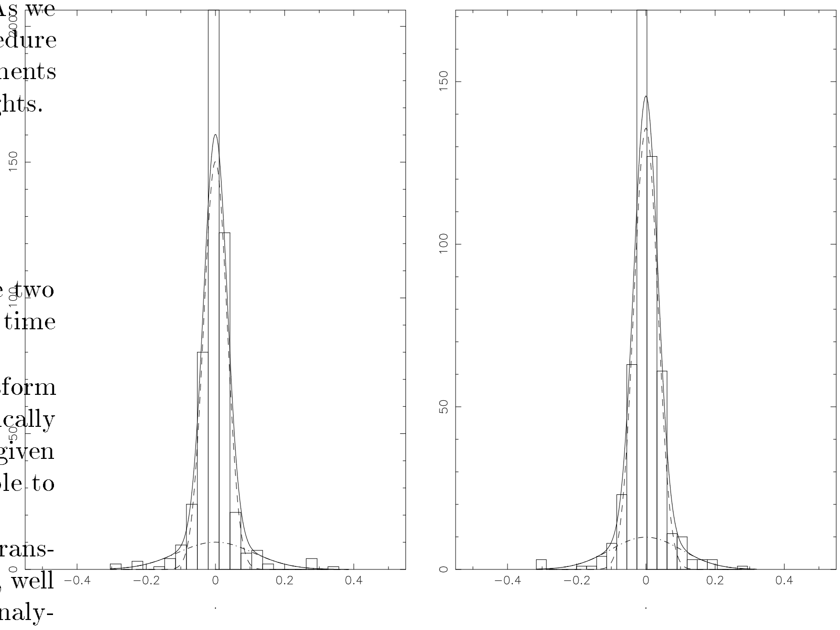

Fig. 10. Histograms of gaps between original data and reconstructed models discriminated at the 3σ-level.
top: Fourier, *bottom*: wavelet
boxes: histograms of data such that $\sigma_i \in \mathcal{S}$
dashed lines: gaussian model for those data such that $\sigma_i \in \mathcal{S}1$
dot-dash-dotted lines: gaussian model for those data such that $\sigma_i \in \mathcal{S}2$
solid lines: gaussian model for those data such that $\sigma_i \in \mathcal{S}$, i.e. sum of the two previous gaussian.

Let us try to quantify, and model this effect. For this purpose, we go back to errors bars of the original time series, as they appear in Fig. 11.

We observe that from point zero to about point 340 errors bars are larger, particularly in winter periods. This is a consequence of the scarcity of measurements and also of the astrolabe adjustment in the early years of operation. The last period (from about point 340) is characterized by significantly smaller errors bars: it comes essentially from having increased the number of prisms and consequently the number of measurements, even in winter periods. Distribution of the σ_i, let us call it $\mathcal{S}$, is plotted in Fig. 12. As a simple test, we shall split this distribution into two sets, a first one for the biggest σ_i, correspond-

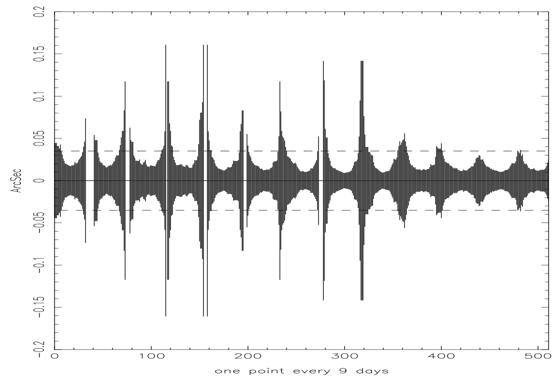

Fig. 11. Actual time series of errors bars centered around zero. Notice the large variety of σ_i's amplitudes and the signature of seasons; the dotted lines correspond to separations between subsets $\mathcal{S}1$ and $\mathcal{S}2$.

ing to winter seasons in early years and a second set for the other, smaller σ_i. Let us take 90-day winters, along about 12 years of measurements, and remembering that we keep one point every 9 days, we arrive at around 120 "winter" points among our 512 points series. Out of those 120 points, 23 of them correspond to no observation at all. They should thus not be considered; so, finally, it remains $120 - 23 = 97$ "winter-like" points. If, starting backwards from the largest uncertainties, we count 97 points in the histogram $\mathcal{S}$, we arrive at the desired value of σ_i for splitting the distribution $\mathcal{S}$ into two sets: $\sigma_i = 0.07$. Let us denote the two subsets of $\mathcal{S}$ by $\mathcal{S}1$ for $\sigma_i < 0.07$ & $\sigma_i \neq 0$ and $\mathcal{S}2$ for $\sigma_i \geq 0.07$ (& $\sigma_i = 0$).

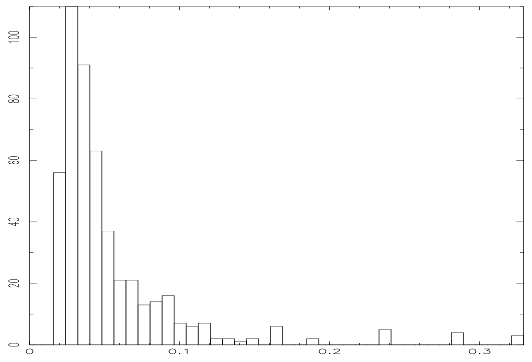

Fig. 12. Distribution $\mathcal{S}$ of data errors bars in the running mean time series of solar radius data.

It remains now to evaluate the rms of data-to-model distances sorted according to their σ_i belonging either to $\mathcal{S}1$ or to $\mathcal{S}2$. From these rms, we may calculate the gaussian distributions which are suited to both subsets. The results are shown on Fig. 10, for the Fourier and for the wavelet models. It can be seen that adding the "winter-type", large gaussian essentially provides the extended wings to the inner distribution which goes with the more precise points. The sum is clearly an adequate representation of the entire histogram, as was expected.

We find that the $\mathcal{S}1$ rms calculated for Fourier and wavelet models are quite similar in both cases, which is visible in Fig. 10. Nevertheless, if one weights the data-to-model distances by $1/\sigma_i^2$, we find that the ratio (Fourier width)/(wavelet width) for $\mathcal{S}1$ points is equal to 3.71 in favor of the wavelet method. Careful examination of Fig. 5 & 9 can explain it: in the first period, where the data are less precise, wavelet makes less effort to fit them. In other words, the 3σ-level is less severe than in the last period. The Fourier model cannot make any distinction between periods. It thus provides uniform quality of fits whatever the data uncertainties. That is why we find a ratio which is so in favour of the wavelet transform.

6. Conclusion

As we have seen, *for the specific time series that we have analysed, and with the error bars that go with this series*, the model that we have obtained through wavelets is to be preferred. First because it automatically leaves out large error bars, as a very efficient razor; and second, because the number of independent parameters being smaller, the representation is simpler, as Occam's razor principle would recommend!

In our opinion, this does not imply that the underlying physics consists of localized wave packets, and not of standing waves. As has been stressed many times, there are numerous solar surface phenomenons which could impinge on the astrolabe solar radius measurements. The corresponding modelizations go from periodical to quasi-periodical, even to chaotic ones. In order to disentangle the possible intrinsic solar radius variations from other effects, one may consider, for example, performing multivariate or correlation analysis between solar radius measurements and other relevant global solar parameters that are currently available. In this respect, we are convinced that such analysis would benefit from being made in the time-frequency plane. In particular, if some time lags would exist between independent sets of data, they would be easy to trace in this plane. This will be the subject of a forthcoming study.

Acknowledgements. We wish to thank especially F. Laclare for having made his precious measurements available to us, and for fruitful discussion during the completion of this work. A. Bijaoui deserves, too, a special mention for his kind advice in wavelet analysis theory and practice, and for his constant interest during completion of this work.

References

ijaoui, A., 1990, internal report.

ijaoui, A., 1991, Ecoles CEA-EDF-INRIA, Rocquencourt, France, June 17-21, 1991.
aubechies, I., 1987, Proceedings of the International Conference, Marseille, France, December 14-18, 1987, 38, 66.
elache, Ph., Laclare, F., 1985, Nat, 6036, 416.
elache, Ph., Laclare, F., Gavryusev, V.& Gavryuseva, E., Regulo C. & Roca Cortes, T. 1993a, ApJ, 407, 801.
elache, Ph., Laclare, F., Gavryusev, V.& Gavryuseva, E. 1993b, Mem. Soc. Astron. Ital., 64, 237.
avryusev, V., Gavryuseva, E., Roslyakov, A., 1991, Sol. Phys., 133, 161.
avryusev, V., Gavryuseva, E., Delache, Ph. & Laclare, F., 1994, A&A, 286, 305.
rossmann, A., Kronland-Martinet, R., Morlet, J., 1987, Proceedings of the International Conference, Marseille, France, December 14-18, 1987, 2, 20.
aclare, F., 1983, A&A, 125, 200.
allat, S.G. 1989, A Theory of Multiresolution Signal Decomposition: The Wavelet Representation, IEEE Transf. on Pattern Anal. and Machine Intell., Vol. 11, No. 7, pp. 674-693.
eyer, Y., 1987, Proceedings of the International Conference, Marseille, France, December 14-18, 1987, 21, 37.

This article was processed by the author using Springer-Verlag LaTeX A&A style file *L-AA* version 3.